eng

MDPI

Article

Staged Wetting and Contact Stress Redistribution Beneath a Segmented Hydraulic Structure on Collapsible Loess

Gulnaz Zhakapbayeva, Saken Uderbayev *, Nargul Saktaganova, Aigul Budikova *, Gulnur Zhakypova, Gulnur Tulegenova and Nurbolat Tursynkozha

Department of Architecture and Construction Production, Korkyt Ata Kyzylorda University, Kyzylorda 120014, Kazakhstan; gulnazzhak.2710@gmail.com (G.Z.); amanovna75@korkyt.kz (N.S.); gulzhak_2025@mail.ru (G.Z.); gul-0922@mail.ru (G.T.); nyrbolat-1997@mail.ru (N.T.)

* Correspondence: saken.uderbayev@gmail.com (S.U.); aigul.budikova@korkyt.kz (A.B.)

Abstract

Wetting-induced collapse of loess can produce large differential movements beneath irrigation structures even under modest nominal foundation pressure. This study investigates the coupled response of a segmented reinforced-concrete chute and its loess-based model foundation in a single 1:50 physical model explicitly interpreted as a 1 g kinematic mechanism test, with simultaneous wetting from the upstream and downstream pools. At corresponding scaled depths, the model-to-prototype geostatic stress ratio is $(\gamma m/\gamma p)/50$, approximately 1/50 for comparable soil unit weights; applied contact loading does not restore the prototype self-weight stress profile. Vertical movement records from eight markers, including an incomplete early Zh record, were evaluated together with contact and embedded pressure-cell measurements. In this test, contact stress at a softened support decreased from 154 to 30 kPa (80.5% unloading), while stress at the adjacent initially dry support increased from 150 to 220 kPa (46.7% amplification). The flume-end stress decrease of approximately 39% is interpreted as being consistent with beam action on a shrinking temporary central support. This support configuration is a proposed explanation of the observations; its pressure and contact area were not measured. Final settlements at the eight markers had a spatial coefficient of variation of 40.2%, describing within-test settlement nonuniformity rather than repeat-test variability or measurement uncertainty. Model settlements of 1.8 and 2.0 cm have geometric equivalents of 0.90 and 1.00 m at a scale factor of 50. Compared with field settlements of 0.76 and 0.93 m, the absolute differences are 0.14 and 0.07 m, respectively, corresponding to point-wise absolute percentage differences of 18.42% and 7.53%. These two comparisons are descriptive and do not validate prototype predictions. The indicator-grid deformation suggests a localized punching pattern, but one with unquantified boundary-location uncertainty. All quantitative findings are specific to this single test. The observed stress redistribution motivates a qualitative staged assessment framework; replication at different initial densities and water contents and independent verification are required before quantitative design application.

Keywords: collapsible loess; hydraulic structure; staged wetting; soil–structure interaction; contact-stress redistribution; differential settlement

Check for updates

Academic Editors: Wanli Yang and Alessio Cascardi

Received: 18 September 2026
Revised: 8 October 2026
Accepted: 14 October 2026
Published: 16 October 2026

Copyright: © 2026 by the authors. Licensee MDPI, Basel, Switzerland. This article is an open access article distributed under the terms and conditions of the Creative Commons Attribution (CC BY) license.

1. Introduction

Loess is a metastable, open-structured aeolian soil whose apparent strength at low water content is sustained by suction, clay bridges, soluble salts, and weak cementation. Under load, wetting weakens these bonds and produces rapid irreversible volume loss [1–5].

This mechanism is especially hazardous in Central Asian irrigation systems because the structure may remain stable after construction, while leakage, initial filling, or routine filtration later triggers highly nonuniform settlement.

The natural loess used to prepare the model mixture originated from the Kyzylorda region, Kazakhstan. Regional evidence is provided by Budikova and Kamalova [6], who investigated hard loess loam from five pits in the Terenozek area of the Kyzylorda region. Their Table 1 reports initial void ratios e_0 = 0.968–0.996, with a mean of 0.981; the sampled loess layers were 3–7 m thick. These published values characterize the sampled regional deposits, not the material used in the present model. That study does not report numerical wetting–collapse coefficients or establish a site-specific Type I/Type II collapsibility classification for those five pits. For the original material used here, the site-specific collapsibility class, coefficient of collapsibility (δs), and initial void ratio remain undocumented. The values δs = 0.067 under natural overburden loading and e_0 = 1.0–1.04 reported elsewhere in this paper refer to the separate Terek–Kuma field-comparison soil in Stavropol Krai, Russia, and are not assigned to the Kyzylorda material or prepared model mixture. The experiment therefore contributes observations of interaction mechanisms under the tested conditions rather than a regional geotechnical classification.

Controlled-suction and oedometer studies show that collapse depends jointly on initial void ratio, stress level, wetting path, and degree of saturation [7–10]. Graded wetting does not simply reproduce flooding at a slower rate: it changes the sequence of bond degradation and pore closure [11]. Recent X-ray and image-based studies confirm that macro-pore loss, particle rearrangement, and destruction of inter-aggregate contacts govern the transition from a metastable to a denser fabric [12,13]. Water-retention behavior also differs between mechanical and hydraulic wetting paths [14], while compressibility evolves continuously across partial-wetting states [15].

Hydraulic conductivity is not constant during this process. Wetting and shearing can reorganize connected pores and alter permeability by orders of magnitude relevant to the advance of the saturation front [16]. Temperature, intact versus recompacted fabric, paleosol interlayers, and repeated wetting–drying histories further modify yield and collapse behavior [17–19]. Coupled hydro-mechanical tests on soft-plastic loess demonstrate that permeability, deformation, and strength must be interpreted along the same stress and moisture path [20]. These findings explain why a collapse strain measured at a single terminal water content cannot describe the complete foundation response.

At the infrastructure scale, spatially progressive wetting creates an additional soil–structure interaction problem. Physical modeling of a tunnel in loess showed that the moving wetting front changes the location and magnitude of deformation [21], while discrete-element simulations reproduced bond breakage and localized collapse under biaxial loading [22]. Inverse analysis of shallow foundations likewise found that settlement predictions are sensitive to the evolution of soil properties during wetting rather than only to their initial values [23]. Bearing-capacity tests in collapsible Khon Kaen loess and analyses of liquid-storage foundations also emphasize the influence of wetting geometry and structural load distribution [24,25].

Simplified prediction methods have related collapse to initial void ratio and moisture content [26], but large fills and reclaimed loess show that placement history and field-scale heterogeneity remain important [27]. Improvement strategies include biologically induced modification [28], cement-kiln-dust stabilization [29], dynamic compaction [30], laboratory-selected treatment schemes [31], and pile-based composite foundations [32]. Such treatments can reduce collapse potential, yet their selection still requires a defensible model of the untreated soil–structure system. Microstructural evidence [33] and standard-

ized collapse-potential testing [34] provide necessary material indices but do not directly quantify transient contact-stress redistribution beneath a segmented hydraulic structure.

Structural stiffness must be considered within existing soil–structure interaction approaches. Mayne and Poulos [35] incorporate foundation rigidity and embedment into elastic settlement influence factors; their formulation supplies a general stiffness framework, not a constitutive law for wetting-induced collapse. Its use for collapsible soils requires independently characterized wetting-dependent soil response. Field monitoring of shallow foundations on tropical collapsible soil by Martins et al. [36] also identified building rigidity as contributing to settlement stabilization; those field conditions differ from the present chute test. Accordingly, the interpretation combines the established role of foundation rigidity with wetting-dependent soil response, while distinguishing individual segment flexural rigidity from joint rotational stiffness. The remaining gap is direct experimental contact-pressure redistribution beneath articulated chutes, not a lack of general stiffness frameworks.

The knowledge gap addressed here is specifically the limited direct experimental evidence of contact-pressure redistribution beneath articulated hydraulic chutes as progressive wetting changes support beneath adjacent segments. It is not a general absence of frameworks for structural stiffness or foundation response on collapsible soils. Conventional layerwise collapse calculations quantify soil deformation, but, unless coupled to a structural interaction model, do not resolve fragment rotation, contact loss, and reaction transfer between connected segments.

The present study addresses this narrowly defined experimental gap using a 1:50 physical model interpreted explicitly as a 1 g kinematic mechanism test. At corresponding geometrically scaled depths, the model-to-prototype geostatic stress ratio is $(\gamma m/\gamma p)/50$, approximately $1/50$ for comparable soil unit weights. External loading specifies nominal contact pressures but does not restore the prototype depth-dependent self-weight stress field. The objectives are therefore to document model-scale movements and local pressure redistribution during imposed two-sided wetting and to interpret changes in support configuration. The analytical punching interpretation and geometric-equivalent field comparisons are descriptive, not validation of prototype deformation predictions. The contribution made is an experimental observation of how support loss in one zone changes the contact pressure in an adjacent zone before its wetting, within the tested configuration.

The observations from this single model experiment suggest that the response beneath a segmented hydraulic structure depends on both the collapse characteristics of the soil and the evolving structural support scheme during wetting. Measured contact pressure locally fell by about 80% and rose by about 47% above its initial value in adjacent zones.

Literature Synthesis and Knowledge Gap

The review comprised 35 research articles and one test standard, including regional Kyzylorda soil characterization [6], an elastic foundation-rigidity framework [35] and field evidence on structural rigidity in collapsible soil [36]. The articles were organized into four connected themes: fundamental collapse mechanisms [1–11], microstructure and coupled hydraulic behavior [12–20], infrastructure-scale response and numerical interpretation [21–27], and foundation improvement or design evidence [28–33]. Table 1 makes the evidence chain and the remaining experimental gap explicit.

Table 1. Synthesis of representative works in the literature and the experimental gap addressed in this study.

Theme and Sources	Main Evidence	Unresolved Issue Addressed Here
Collapse mechanism [1–5]	Wetting destroys metastable bonds and produces irreversible volume loss.	No transient contact-pressure measurements beneath segmented structures.
Controlled wetting [7–11]	Collapse depends on stress, void ratio, suction, and wetting path.	Applied stress changes during progressive wetting were not tracked.
Microstructure [12,13,15,19,33]	Macro-pore loss and contact rearrangement explain fabric collapse.	Element-scale fabric evidence requires structural-scale validation.
Hydraulic coupling [14,16–20]	Retention, permeability, temperature, and cycling alter yielding.	Few tests link the moving front to load transfer between supports.
Infrastructure response [21–25]	Wetting geometry governs tunnel and shallow-foundation deformation.	Rigid hydraulic fragments and joint rotation remain underrepresented.
Prediction [26,27]	Initial state and placement history control predicted settlement.	One-dimensional sums omit changing beam and cantilever schemes.
Improvement [28–32]	Biological, chemical, compaction, and pile methods reduce collapse.	Treatment extent requires the active collapse-zone depth.

2. Materials and Methods

2.1. Prototype and Modelling Approach

The prototype was a three-part reinforced-concrete chute comprising an inlet, a sloping water-conveying flume, and a stilling basin. Its overall length was 36 m, design discharge 4.0 m^3/s, and elevation drop 3.5 m; the collapsible loess stratum reached 19 m. The laboratory model was constructed at a geometric scale of 1:50 and tested under normal gravity (1 g), explicitly as a kinematic mechanism test with distorted geostatic stresses. The apparatus is a 1 g physical model designed to measure kinematically driven contact-stress redistribution beneath the loaded structural footprints as wetting causes support deformation, segment movement, and changes in contact. It does not achieve complete geotechnical similitude (Table 2).

Table 2. Prototype and model parameters. Note: all tabulated lengths are in meters. The geometric scale is Lmodel/Lprototype = 1/50; 1 cm = 0.01 m. Equal nominal applied pressures do not establish complete stress similitude.

Parameter	Prototype	Model
Linear scale	1.00	0.02
Overall structural concept	Three rigid fragments	Three rigid fragments
Loess thickness below inlet	16.5 m	0.33 m
Loess thickness below basin	13.0 m	0.26 m
Model-box width	-	0.21 m
Inlet foundation width	2.5 m	0.05 m
Basin foundation width	3.5 m	0.07 m
Nominal inlet foundation pressure	150 kPa	150 kPa

Loading was applied using a combined arrangement. Calibrated steel discs weighing 20–40 kg were suspended beneath a rigid steel table. Force was transmitted through paired lever arms and vertical rods passing through guide sleeves to two loading platens with centering balls. One platen loaded the horizontal inlet segment; the other acted on a horizontal beam distributing force to the two lateral surcharges in the downstream excavation. Additional loads and surcharges were applied using steel weights placed directly on the model. The prescribed nominal pressures were 150 kPa beneath the inlet

incorporating the crossing, 32 kPa beneath the stilling basin, and 15 kPa beneath the sloping flume. Lateral surcharges ranged from 36 to 45 kPa upstream and from 45 to 108 kPa downstream. These prescribed loads are distinct from the local contact pressures, which redistributed during wetting.

The original loading design accounted approximately for prototype soil self-weight by considering the calculated total vertical stress distributions from structural loading, lateral surcharges, and overburden. These distributions were approximated by rectangular profiles over adopted compressible depths of 7.0 m beneath the inlet and 5.5 m beneath the basin, with average total vertical stresses of approximately 110 and 90 kPa, respectively. This approximation informed the loading scheme but did not reproduce the complete prototype stress profile. These average subsurface stresses are distinct from the prescribed foundation pressures.

All scale ratios are defined as model/prototype. Self-weight vertical stress scales according to

$$\sigma_{v,g} = \rho g z; \quad \lambda_{\sigma,g} = \lambda_\rho \, \lambda_g \, \lambda_L$$

For a geometric scale of 1:50 under normal gravity, achieving a nominal stress ratio of unity would require

$$\lambda_\rho = \frac{\lambda_\sigma}{\lambda_L \, \lambda_g} = \frac{1.0}{0.02 \times 1.0} = 50$$

The natural soil does not provide this density ratio. For comparable model and prototype densities,

$$\lambda_\rho \approx 1; \quad \lambda_{\sigma,g} \approx 0.02 = \frac{1}{50}$$

At corresponding geometrically scaled depths, the self-weight stress relationship for a homogeneous profile with comparable densities is

$$z_m = 0.02 \, z_p; \quad \sigma_{v,g,m}(0.02 \, z_p) \approx 0.02 \, \sigma_{v,g,p}(z_p)$$

The resulting absolute self-weight stress deficit, expressed at the corresponding prototype depth, is

$$\Delta\sigma_{v,g}(z_p) = \sigma_{v,g,p}(z_p) - \sigma_{v,g,m}(0.02 \, z_p) \approx 0.98 \, \rho_p g z_p$$

The stress ratio is approximately constant, but the absolute self-weight stress deficit increases with depth. Applied structural loads and lateral surcharges do not restore the prototype geostatic stress profile. Multiplication of model settlements and punching-zone depths by 50 gives descriptive geometric equivalents, not validated prototype predictions. Seepage time was not scaled.

2.2. Model Soil and Preparation

The model foundation was prepared from crushed and sieved natural loess aggregates from the Kyzylorda region, Kazakhstan (0.1–2 mm), mixed with fine quartz sand at an air-dry mass ratio of 1:0.66, equivalent to approximately 60.2% loess aggregates and 39.8% added sand. Aggregate sizes and mixture proportions are preparation specifications, not a complete primary-particle size distribution. The available experimental description does not provide hydrometer/sieve percentages of primary clay, silt, and sand particles (Table 3).

The mixture was conditioned in desiccators to a preparation water content of 0.08 and placed in 2 cm layers. Each layer was compacted using a standard DorNII apparatus to a target bulk density of 1.50 mg/m^3. If this target density and preparation water content are treated as paired values, the implied dry density is $\rho d = \rho/(1 + w) = 1.50/1.08 \approx 1.39$ mg/m^3; this is a calculated preparation value, not a separately documented measurement. The

previously stated initial water content of 0.12 could not be reconciled with the source preparation record and is not retained as a verified initial condition. No separate model void-ratio measurement or specimen-specific model particle density is available.

Table 3. Soil-characterization matrix distinguishing the prepared model mixture, archival Terek–Kuma field soil, and independent works in the regional Kyzylorda literature [6]. Missing measurements are identified explicitly; field and regional values are not assigned to the model mixture. Archival model and field data: Zhakapbayeva (2001) [37].

Property/Condition	Prepared Model Mixture	Terek–Kuma Field Soil (Archival Source)	Regional Kyzylorda Loam [6] (Independent Literature)
Material/provenance	Kyzylorda loess aggregates mixed with quartz sand	Strongly collapsible loess-like sandy soil	Hard loess loam; five Terenozek pits; layer thickness 3–7 m
Composition/preparation	Air-dry loess:sand mass ratio 1:0.66; 2 cm layers; DorNII compaction	Natural profile; intact reference soil	Natural monolith samples
Initial water content w	0.08, source-reported preparation target; former 0.12 unverified	≈0.08, profile summary	7.6–8.6%; mean 8.14%
Bulk density ρ	Target 1.50 mg/m^3; achieved distribution undocumented	≈1.50 mg/m^3	1.480–1.504 mg/m^3; mean 1.491 mg/m^3
Dry density ρd	≈1.39 mg/m^3, calculated as 1.50/1.08; not independently measured	≈1.40 mg/m^3	Mean initial value 1.378 mg/m^3, Table 2 at p = 0
Particle density ρs	Not separately documented	2.70 mg/m^3	2.70–2.75 mg/m^3; mean 2.73 mg/m^3
Initial void ratio e_0	Not separately documented; regional values not assigned to mixture	Reported 1.0–1.04; densities imply ≈0.93; not paired specimen data	0.968–0.996; mean 0.981
Liquid limit wL	Not separately documented	23%	25–28%; mean 26.74%
Plastic limit wP	Not separately documented	18%	16–18%; mean 16.92%
Plasticity index IP	Not separately documented	5 percentage points, calculated	9.82 percentage points, calculated from reported mean limits
Primary-particle size distribution	Complete clay/silt/sand fractions unavailable	Complete distribution unavailable in inspected source	Complete distribution not tabulated in [6]
Aggregate size/added sand	Loess aggregates 0.1–2 mm; added fine quartz sand; aggregate size is not primary-particle gradation	Not applicable	Not applicable
Pre-wetting friction angle φ	No separately documented model-mixture value	23–25°, natural-state source summary	Not numerically reported in [6]
Pre-wetting cohesion c	No separately documented model-mixture value	10–12 kPa, natural-state source summary	Not numerically reported in [6]
Collapse-stage shear parameters	φ = 19°, source-reported; test details unavailable. c = 0 kPa, analytical assumption	Natural-state values are not collapse-stage parameters	Not assigned to the model
Coefficient of collapsibility δs	Separate numerical value unavailable; source collapse curves informed selection	Depth-averaged 0.067 under natural overburden loading	Numerical wetting–collapse coefficient not reported in [6]
Collapse-initiation pressure	Separate numerical value unavailable	25 kPa, profile summary	Not reported in [6]
Hydraulic conductivity	Not separately documented	0.16–0.28 m/day (≈1.85–3.24 × 10^{-6} m/s); method/direction unspecified	Not reported in [6]
Compression modulus	No value with defined stress interval and moisture state documented	No such numerical value documented in account inspected	No modulus adopted from [6]

Table 3. *Cont.*

Property/Condition	Prepared Model Mixture	Terek–Kuma Field Soil (Archival Source)	Regional Kyzylorda Loam [6] (Independent Literature)
Model–field response comparison	Source collapse curves used for mixture selection; numerical coordinates, repeats and separate compression curves unavailable	Reference collapse response; not proof of complete similitude	Independent regional context; not a calibration dataset
Wetting-state water contents	Front: 0.27; wetted zone: 0.30; source estimates, sampling details unavailable	Not assigned from model values	Not assigned from model values
Wetting-state saturation	Front: 0.73; wetted zone: 0.85; source estimates	Not assigned from model values	Not assigned from model values
Local stabilization/quality control	About 2 days after local wetting; compaction energy, density/moisture tolerances and spatial checks undocumented	Not a model preparation condition	Independent literature samples; not model quality-control measurements

The separate Terek–Kuma field-comparison soil was described as a strongly collapsible, light silty loess-like sandy soil, with liquid and plastic limits wL = 0.23 (23%) and wP = 0.18 (18%); the corresponding calculated plasticity index is IP = 0.05 (5 percentage points). The source summarizes bulk density as 1.50 mg/m^3, dry density as approximately 1.40 mg/m^3, particle density as 2.70 mg/m^3, and void ratio as 1.0–1.04. These profile-summary values are not internally consistent as paired specimen data: the reported dry and particle densities imply e $\approx$ 0.93. The stated void-ratio range is therefore reported as a source value rather than used to calculate a model property. No complete prototype particle-size distribution is available in the experimental description inspected.

The 2 cm placement layers and standard DorNII compaction apparatus are documented, but the number of blows, compaction energy, and acceptance tolerances are not. The preparation water content of 0.08 and target bulk density of 1.50 mg/m^3 are source-reported targets rather than a verified distribution of measured values throughout the box. Records of water addition, moisture equilibration, layer-by-layer density and moisture checks, and spatial uniformity verification are unavailable. The calculated dry density therefore does not establish achieved uniformity.

The preparation procedure was designed to match wetting-induced collapse response, because crushing the intact loess increased its collapse tendency and adding quartz sand reduced it. The original comparison of collapse-strain versus stress curves (illustration numbered 3-2 in the source dissertation [37]) includes intact prototype soil, crushed soil, and the selected mixture. The source reports depth-averaged prototype relative collapse strain (coefficient of collapsibility, δs) = 0.067 under natural overburden loading and collapse-initiation pressure psl = 25 kPa for the collapsible profile. These are prototype profile summaries, not separately measured properties of the prepared model mixture. The source describes the selected mixture as matching the prototype collapse response; however, numerical curve coordinates, repeat-test scatter, and a separate comparison of compression curves are not available here. The identification of the model material as a collapsible loess-based mixture is supported by the source comparison of wetting–collapse curves used for mixture selection and the settlement observed during wetting in this experiment. These observations support collapse susceptibility but do not provide a complete independent geotechnical characterization of the mixture.

The source reports a prototype permeability coefficient of 0.16–0.28 m/day (approximately 1.85–3.24 $\times$ 10^{-6} m/s). This is a profile-summary range for the natural foundation soil; the measurement method and directional dependence are not specified in the available account. No separately measured permeability coefficient is documented for the prepared model mixture. Neither a soil–water characteristic curve nor a numerical compression

modulus with a specified stress interval and moisture condition is available for the model mixture or corresponding prototype in the inspected experimental description. Consequently, no model hydraulic conductivity, retention parameters, or compression modulus is assigned. Atterberg limits reported for the prototype soil must not be attributed to the crushed-loess–sand mixture, for which separate limits are unavailable.

The friction angle of 19° is described in the original experimental account as experimentally established during collapse. The test method, drainage conditions, specimen details, and uncertainty are not specified in that account; it is therefore treated as a source-reported parameter for the analytical comparison, not a fully documented effective-stress strength parameter. Cohesion c = 0 kPa was adopted as an analytical idealization of weakened remolded soil during wetting-induced collapse, rather than measured as zero. The prototype natural-state values reported in the source (φ = 23–25° and c = 10–12 kPa) refer to a different soil condition and should not be equated with the collapse-stage assumptions.

During placement, horizontal and vertical indicator bands of finely ground colored chalk were installed. Horizontal bands were spaced at 4 cm; vertical bands were positioned beneath the inlet foundation edges and at 1 cm increments outside them. The displaced grid was examined after the test to identify the model deformation pattern.

2.3. Instrumentation and Wetting Protocol

Miniature strain-gauge total-pressure cells were installed at the soil–structure contact and at 4 cm intervals along selected vertical profiles. Cells S1, S2, and S9 monitored the inlet contact; S10 and S12 monitored the flume ends; S3–S6 measured vertical stress with depth; and S7–S8 measured lateral stress. Each metal cell had an outer diameter of 24 mm, a 20 mm sensing membrane, and an 8 mm height. Two wire strain gauges were connected in a half-bridge to an AID-4 deformation indicator. Individual deformation–pressure calibration curves were used to convert readings to pressure, and initial readings were recorded after assembly. Surface settlement was read to 0.01 mm; the available marker records are listed in Table 4.

The source includes an example loading–unloading calibration plot for cell No. 18, extending from zero to approximately 400 kPa. The two branches show hysteresis. This plotted calibration span is not a certified measuring range for every cell. Calibration coefficients, reference-load accuracy, repeatability, drift, and numerical residuals for individual cells are unavailable in the supplied record; an absolute pressure accuracy or expanded uncertainty therefore cannot be specified.

The cells were purpose-built metal diaphragm instruments; no commercial model designation is reported. Contact cells were installed beneath the structural segments. Embedded cells were arranged at 4 cm depth intervals along a central vertical line to measure vertical normal stress and along an edge vertical line, with the sensing faces oriented vertically, to measure horizontal normal stress. Leads ran horizontally to the rear wall and then through vertical polyethylene tubes, with slack loops to accommodate settlement. Initial readings were checked and recorded after assembly. The source does not document local bedding, seating checks, installation-induced soil disturbance, or the precise loading medium and procedure used to produce the individual calibration curves.

No cell–soil stiffness matching correction or quantitative correction for box confinement was documented. Diaphragm compliance relative to the surrounding soil can change local load transfer: stress may concentrate on a comparatively stiff inclusion or be diverted around a more compliant one. Local arching around the cells and load transfer to the rigid box walls could therefore bias the recorded stresses. Neither their magnitude nor their sign can be determined from the available calibration record. Changes in soil stiffness during wetting also mean that this bias need not remain constant, so normalization by

initial readings cannot be assumed to eliminate it. The readings are interpreted as local total-stress responses of the instrumented, confined model; their absolute magnitudes and percentage changes are reported descriptively, without a quantified uncertainty or a claim of unbiased prototype pressure measurement.

Table 4. Vertical displacement history of model markers. Archival model and field data: Zhakapbayeva (2001) [37]. (**a**) Source-reported wetting-front sequence and associated model response; positions are relative descriptions, not measured front coordinates.

Day	B	A	V	G	D	E	Zh	I
1	0.6	0.6	0.5	0.0	0.0	0.0	-	0.3
2	2.1	1.3	1.0	0.5	0.0	0.0	-	0.7
3	3.5	2.7	2.5	1.6	0.3	0.7	0.9	1.2
4	4.4	3.8	3.4	2.6	1.9	1.4	1.7	1.9
6	4.50	3.86	3.55	2.81	2.01	1.50	1.80	2.0
7	4.50	3.87	3.55	2.81	2.00	1.50	1.79	2.0

(**a**)

Date/model day	Reported wetting-front position	Instrument evidence/interpretation
25 July/initiation	Wetting introduced at both end compartments.	Initial S1 contact pressure 154 kPa; dry-reference condition.
26 July/day 1	Upstream wetted region beneath the inlet outer end; opposing wetting from downstream.	S1 decreased to 110 kPa; marker B 0.6 cm, G 0.0 cm: differential support.
27 July/day 2	End regions continued wetting; basin response described as the mirrored inlet mechanism.	S1 decreased to 30 kPa; S9 reached 220 kPa during dry-side load transfer; exact peak timing not independently digitized.
28 July/day 3	Contours advanced beyond the inlet downstream end and the basin upstream end.	Source reports end-contact stresses recovering toward initial values; transitional support configuration.
29 July/day 4	Opposing fronts approached/met beneath the flume center, according to the source narrative.	S10/S12 reported to decrease from 110–115 to 67–70 kPa. A central support is inferred; its water content was not measured. S11 had failed.
30 July/day 5	Later contours extended deeper through the foundation.	Settlement records approached stabilization; no independently verified date of complete foundation saturation.

Note: Values are in centimeters; day 1 began on 26 July after wetting started on 25 July. A dash indicates an unavailable reading. Zh readings for days 1 and 2 are missing and have not been interpolated.

Wetting started on 25 July simultaneously from upstream and downstream water compartments with perforated inner walls. Two water-supply vessels maintained the pool levels, as shown in the original apparatus photographs. The maintained water-surface elevations and pressure heads relative to a stated datum, as well as their fluctuations, were not numerically recorded in the available account. Consequently, no verified hydraulic-head values are assigned here. The rigid acrylic walls and base formed the mechanical container boundaries; the basal drain, drainage layer, outflow rate, and detailed hydraulic sealing arrangement are not documented. The test therefore cannot be described as having verified fully drained or undrained conditions. This procedure represents imposed two-sided wetting with replenished water supply, rather than an internal leak with a restricted water volume. It was used to examine changes in support and contact stress as wetting progressed; it does not reproduce the hydraulic boundary conditions of a localized operational leak.

The wetting front was identified visually from the pronounced color contrast between wetted and dry soil through the transparent side wall, using its coordinate grid. The original dated contours cover 26–30 July. These are observations at the wall, not measurements of the complete three-dimensional moisture field. Numerical front-coordinate records and a front-location accuracy assessment are not available. The account reports water contents of 0.27 at the visible boundary and 0.30 within the wetted zone, with corresponding degrees

of saturation of 0.73 and 0.85. It does not specify sampling locations, sampling times, or the water-content measurement method; these values are therefore source-reported estimates and are not presented as a reproducible moisture-monitoring dataset. No gravimetric or sensor-based method is assumed retrospectively.

The source documents level-maintaining supply vessels, but not the numerical head setpoint or tolerance, inflow/outflow measurements, flow-rate regulation, or the water balance. Constant-head supply must therefore not be interpreted as constant or measured flow. The visual front record and instrument dates permit qualitative correlation; they do not support reconstruction of hydraulic conductivity, a quantified saturation field, or a hydraulic time-scaling law. The laboratory model, loading apparatus, and reconstructed experimental arrangement are shown in Figure 1.

Table 4a summarizes the documented front positions relative to structural regions and the associated instrument response. A comparatively dry central support is an interpretation supported by the observed front sequence and unloading at the flume ends. Its spatial extent, duration, and internal water content were not independently measured; a fully dry core cannot be confirmed from wall observations alone. The mechanical stages are consequently qualitative interpretations rather than quantitatively verified hydraulic stages.

The three model segments were made of 1 cm thick acrylic sheet, with upper covers added to increase rigidity; the prototype was reinforced concrete. They were connected using bituminous adhesive joint filler with a fibrous additive. A polyethylene membrane was attached at the upper end of the flume. The model flume slope was 0.20. The original account gives a box length of 80 cm, external width of 25 cm, and clear soil width of 21 cm. Box height is inconsistent between the source text (35 cm) and setup drawing (38 cm); no single verified overall height is asserted here. The consistently reported soil thicknesses beneath the inlet and basin are 33 and 26 cm.

The container was constructed from thick transparent acrylic (organic glass), as stated in the original apparatus description. The soil was placed against its rigid vertical walls and base. The surface finish, roughness, and wall thickness were not quantified in the available record. No boundary-lubrication procedure, double-layer PTFE membrane, silicone grease application, measured interface friction angle δ, or interface friction coefficient $\mu = \tan \delta$ is documented; these treatments and values cannot be assigned retrospectively. During downward soil displacement, friction at a vertical wall can transfer upward shear to the soil and divert part of its vertical load to the container. In a simplified Coulomb representation, the limiting interface shear stress is $\tau_{lim} = \sigma_n \tan \delta = \mu \sigma_n$, where σ_n is the compressive normal stress on the wall (the local horizontal normal stress for a vertical interface). Actual mobilized shear need not reach this limit; it depends on relative displacement and interface conditions. The soil friction angle of 19° is not a measured wall–soil interface angle and is not substituted for δ. Neither wall shear nor its variation during wetting was measured, so no quantitative wall-friction correction is made. The walls also restrained displacement normal to their surfaces, and the rigid base restrained downward displacement at the bottom. These effects could suppress lateral spreading, change confinement and stress transmission, and alter measured local contact-pressure redistribution. Although the original width selection aimed to reduce boundary influence, its effectiveness was not verified by tests at different box widths or interface conditions. The magnitude and net effect of the resulting measurement bias cannot be quantified, and the measured redistribution is interpreted as the response within this confined setup.

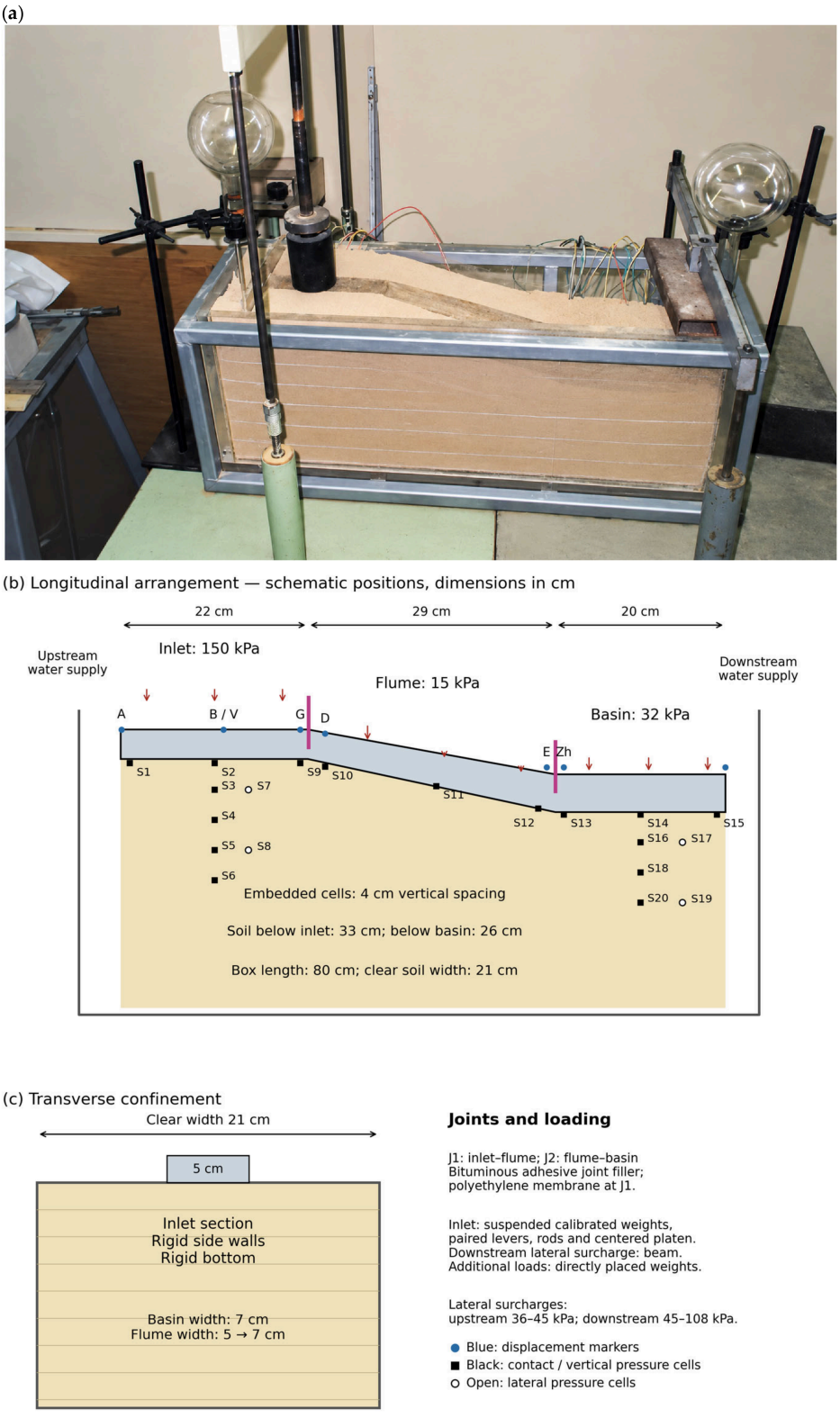


Figure 1. (**a**) Photograph of the laboratory model and loading apparatus. (**b**,**c**) Reconstructed experimental arrangement and transverse confinement based on the original setup drawing. Sensor and marker positions are schematic, not surveyed coordinates; paired B/V markers project to the same longitudinal region. Segment lengths are 22, 29 and 20 cm; the inlet and basin widths are 5 and 7 cm, and the flume widens between them. Black squares indicate contact or vertical cells; open circles indicate lateral cells. The source drawing shows additional instruments not plotted in the present result histories. Joint filler and the inlet–flume membrane are indicated in the legend. Red downward arrows indicate the applied vertical loading; black double-headed arrows indicate dimensions.

2.4. Evaluation Criteria

The experiment was assessed through surface movements, pressure-cell changes, the indicator-grid deformation pattern, and descriptive field comparisons. Geometric-equivalent lengths were calculated as Leq = 50 Lm. This conversion does not establish deformation similitude. For the indicator-grid depth, subtracting mean inlet settlement changes the reference from the initial footing level to the mean final footing level; it does not correct the model physics or establish a prototype punching depth.

2.5. Data Reduction and Uncertainty Control

Settlement readings were reduced relative to the pre-wetting datum for each marker. Contact pressures are local cell readings; changes and ratios are descriptive indicators of redistribution.

The 0.01 mm displacement-reading resolution is not an accuracy specification for the pressure cells. Pressure uncertainty includes calibration residuals and hysteresis, indicator resolution, drift, installation effects, and nonuniform contact over the finite sensing membrane. The available record does not quantify these contributions, so no numerical pressure confidence interval is assigned. Normalizing readings by their initial values can cancel a constant multiplicative calibration factor but does not remove offset, drift, hysteresis, or installation errors. Density variations and visual wetting-front location add further uncertainty. The stress records support an interpretation of redistribution, while quantitative equilibrium closure and the significance of small pressure differences remain unverified.

Scaling was limited to geometric conversion. Pressure-cell values are model measurements and are not assigned a universal prototype stress scale. The experiment did not reproduce the prototype self-weight stress profile, and a unit strain scale was not demonstrated. The reported days describe model events only because permeability, drainage length, and boundary supply were not simultaneously scaled. The directly supported outputs are the model deformation pattern, measured model settlements and stress changes, and the observed indicator-grid geometry.

2.6. Derived Response Metrics

The measured extrema were converted into dimensionless response metrics to permit comparison between cells with different initial readings. The stress ratio, $R\sigma$, was defined as the extreme stress divided by the initial stress of the same cell. Stress amplification was calculated as (maximum − initial)/initial, and unloading as (initial − minimum)/initial. Final settlements at the eight reported markers were summarized by the mean, sample standard deviation, range, and coefficient of variation; these statistics describe spatial nonuniformity and do not represent replicated specimens. At each of the two available field locations, the absolute settlement difference is defined as $\Delta s = |s_{geometric} - s_{field}|$ and the point-wise absolute percentage difference as $100\Delta s/s_{field}$. No average error metric is used. These differences are descriptive comparisons, not measurement-error estimates or validation of prototype predictions.

2.7. Structural Stage Classification

Four interpretive stages were used: initial support, support loss near an end, possible temporary central support, and the condition after the main settlement developed. Stage assignments used the direction of pressure-cell changes, marker movements, and source-reported wall wetting traces together. They are qualitative classifications; numerical transition thresholds and central-core moisture were not measured. For visual comparison, the stress-history plots use approximate date guides at wetting initiation (25 July), 28 July, and 29 July.

These summarize the recorded sequence rather than define measured thresholds; temporary central support is inferred, and stage timing may differ between segments.

The classification describes the observed model response rather than a constitutive model. Engineering implications and the qualitative assessment framework are discussed separately in Sections 4.1–4.4.

3. Results

3.1. Development of Wetting and Settlement

The visible wetting fronts advanced downward and inward from both pools. The original account describes wetting beneath the flume center on the fourth day after initiation (29 July); the same date is described as the meeting of the opposing fronts. These observations delimit a transition around 29 July, rather than proving continued dryness of the central soil beyond that date. The reported water contents (0.27 at the front and 0.30 behind it) and degrees of saturation (0.73 and 0.85) lack a documented measurement protocol. Local movements generally stabilized within about two days of the reported local wetting (Table 4 and Figure 2). The available dated relationships are summarized in Table 4a. The approximately two-day local stabilization and fourth-day arrival of the visible fronts at the flume center are model-test observations, not field time scales. The principal wetting and settlement response developed over approximately 5–6 days, while the plotted stress record extends from 25 July to 1 August. This distinction separates the main response interval from the available observation window.

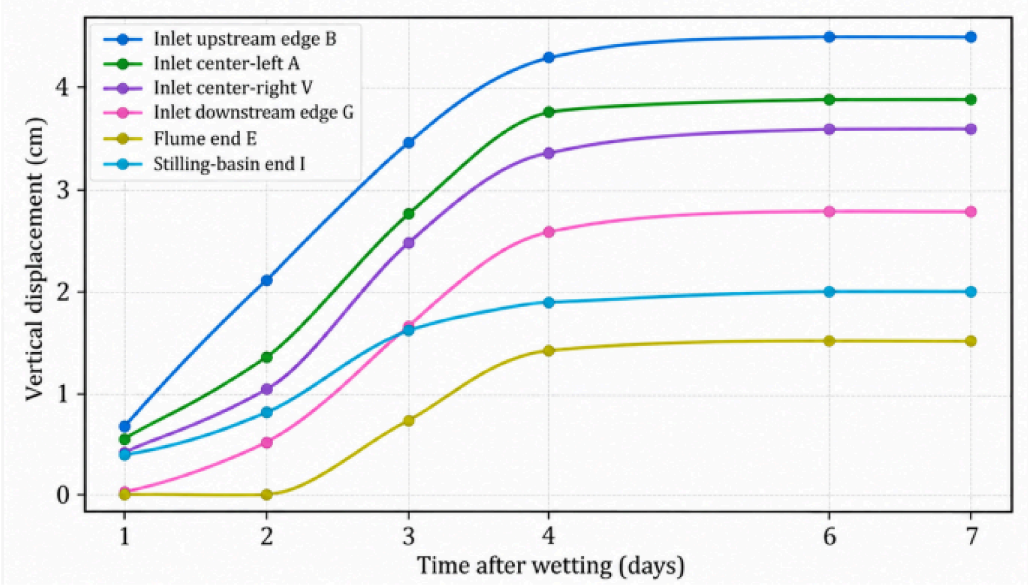


Figure 2. Development of vertical movement at representative model markers.

3.2. Contact Stress Redistribution

The initial contact stress at S1 was 154 kPa. One day after local wetting, it decreased to 110 kPa, and then to 30 kPa. At the same time, the opposite end of the inlet had not settled and S9 increased to 220 kPa. The inlet therefore behaved temporarily as a cantilever fixed in the dry soil. As the wetting front passed beneath the supported end, the contact distribution reversed and subsequently returned toward the initial stress level.

A comparable redistribution sequence occurred beneath the stilling basin. At the flume ends, the source narrative reports S10/S12 decreasing from 110–115 kPa to 67–70 kPa on 29 July, when the opposing wetting fronts approached the center. Figure 3b presents approximate readings recovered from the original graph; its 29 July minima are about 60–65

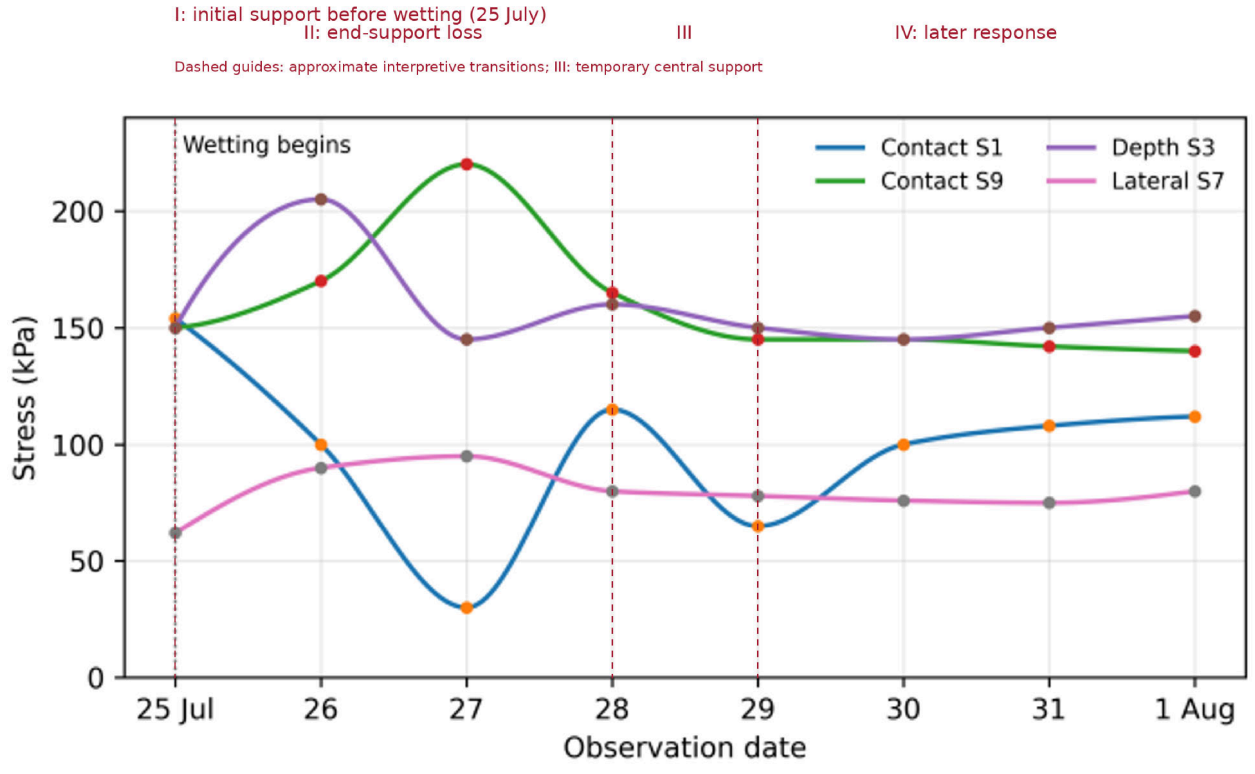
kPa. This difference between the narrative and plotted record is retained explicitly because the original numerical logs are unavailable. S11, located at the center, failed. The end unloading and small end settlements are consistent with a temporary central support, but neither its pressure nor its contact area was measured. The previously quoted 180–200 kPa was an unverified inference and is excluded from the quantitative findings.

For an idealized three-zone vertical-reaction model of the flume, force and moment equilibrium require $R_1 + Rc + R_2 + J_1 + J_2 = W$ and $R_1x_1 + Rcxc + R_2x_2 + J_2L + M_1 + M_2 = WxW$, taking moments about the upstream end. Here, W is the total downward load, including segment self-weight; J_1 and J_2 are signed upward joint forces; M_1 and M_2 are signed joint moments; and R_i and x_i are soil-reaction resultants and their lever arms. Thus, the mean central pressure would be $pc = Rc/Ac = (W - J_1 - J_2 - R_1 - R_2)/Ac$.

Each reaction must be obtained by integration over its actual contact area, $R_i = \int A_i p(x,y)dA$; a local cell reading is not an area-averaged pressure. The full flume footprint is $0.29 \times (0.05 + 0.07)/2 = 0.0174\ m^2$, whereas the central contact area Ac is unknown. The end contact areas, reaction locations, and joint forces/moments were not recorded. S10/S12 alone therefore cannot close force and moment equilibrium or determine a unique central pressure. No numerical reactions or central contact area values were back-calculated from the discarded estimate.

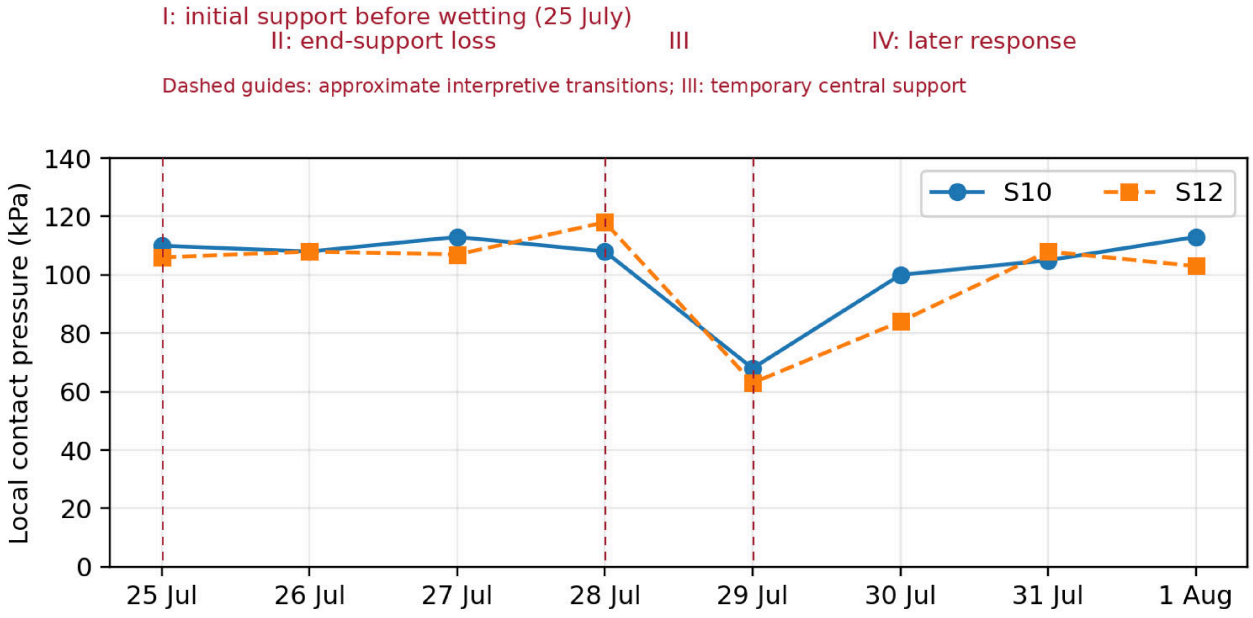
Table 5. Key measured stress transitions.

Location	Initial	Extreme	Interpretation
Inlet, S1	154 kPa	30 kPa	Softened wetted support
Inlet, S9	150 kPa	220 kPa	Load transfer to dry support
Flume ends, S10/S12	110–115 kPa (narrative)	67–70 kPa (narrative)	End unloading; central support inferred
Vertical cells, S3–S6	145–150 kPa	190–205 kPa	Front-induced stress pulse
Lateral cells, S7/S8	62–68 kPa	76–80 kPa stabilized	Post-collapse confinement



(**a**)

Figure 3. *Cont.*



(**b**)

Figure 3. (**a**) Representative contact, vertical, and lateral stress histories. Red dashed guides mark approximate interpretive transitions: Stage I precedes wetting on 25 July; Stage II covers early end-support loss; Stage III represents the temporary central-support interpretation around 28–29 July; Stage IV denotes the later response from approximately 29 July. These guides are not measured transition times; stages can overlap between segments. Source: Zhakapbayeva (2001) [37]; redrawn or reconstructed for the present article. (**b**) S10/S12 flume-end records approximately digitized from the original plotted history (25 July–1 August 2000). Values are rounded graphical estimates, not recovered raw readings; connecting lines guide the eye. The plotted minima are about 60–65 kPa, whereas the source narrative gives 67–70 kPa. Digitization and instrument uncertainties have not been quantified. Red dashed guides mark approximate interpretive transitions: Stage I precedes wetting on 25 July; Stage II covers early end-support loss; Stage III represents the temporary central-support interpretation around 28–29 July; Stage IV denotes the later response from approximately 29 July. These guides are not measured transition times; stages can overlap between segments. Source: Zhakapbayeva (2001) [37]; redrawn or reconstructed for the present article. The key measured stress transitions are summarized in Table 5.

3.3. Stress Transmission Through the Loess

Vertical cells S3–S6 changed synchronously with the contact cells, showing that the redistribution propagated through the active foundation depth. Passage of the wetting front caused a short-lived stress pulse near 190–205 kPa, consistent with load concentration at the interface between softened wet soil and stiffer dry soil. During the later settlement stage, vertical stress in the column beneath the footing stabilized near the applied 150 kPa.

The pressure cells measured total normal stresses; no pore-pressure correction was applied. Before wetting, the reported lateral total stresses were 62–68 kPa. Relative to the reported vertical total stress of approximately 150 kPa, these give a descriptive ratio of 0.41–0.45 (about 0.43). After collapse, lateral total stresses of 76–80 kPa give a ratio of 0.51–0.53 (about 0.52). These are ratios of reported total-stress values, rather than measured effective-stress earth-pressure coefficients (Table 6).

The reported degrees of saturation, 0.73–0.85, indicate partially saturated conditions. Pore-water pressure, pore-air pressure, and matric suction were not measured, and no soil-water retention curve was available to infer suction. Degree of saturation alone does not specify these quantities. Neither zero pore-water pressure nor zero suction is assumed, and the effective stresses and suction contribution to strength cannot be reconstructed.

Wetting-related changes in suction and pore pressure may have influenced the measured total stresses, but their contributions cannot be separated from structural load redistribution and confinement.

Table 6. Reported total stresses and descriptive lateral-to-vertical ratios; no effective-stress limit-state verification.

Quantity	Reported Total-Stress Value	Interpretation
Vertical total stress used as reference	Approximately 150 kPa	Reported reference; no pore-pressure correction
Lateral total stress before wetting	62–68 kPa	Local pressure-cell readings
Initial total-stress ratio	0.41–0.45 (about 0.43)	Descriptive ratio to 150 kPa
Lateral total stress after collapse	76–80 kPa	Local pressure-cell readings
Post-collapse total-stress ratio	0.51–0.53 (about 0.52)	Descriptive ratio; not an effective-stress coefficient
Rankine reference, $\varphi = 19^\circ$, $c = 0$	$K_a \approx 0.51$	Idealized comparison only; active state not established

For reference only, the Rankine expression $K_a = (1 - \sin\varphi)/(1 + \sin\varphi)$ gives approximately 0.51 for $\varphi = 19^\circ$ and zero cohesion. This idealized active-state expression requires sufficient lateral deformation to mobilize an active condition. The model soil was confined by the surrounding soil and rigid box boundaries, and sufficient lateral displacement or shear mobilization was not demonstrated. Ka is therefore not adopted as the governing coefficient for this zone. The reported 19° also lacks documented test conditions and cannot be established here as an effective-stress friction angle. Numerical proximity between the total-stress ratio 0.52 and the theoretical value 0.51 does not verify an active or limiting state; no such conclusion is drawn. An at-rest coefficient is likewise not assigned without a documented lateral strain and stress path.

3.4. Field and Analytical Comparison

The field comparison concerns an experimental reinforced-concrete chute built in 1980 by the Foundations Department of the Moscow Hydromelioration Institute (MGMI) at the second-stage Terek–Kuma irrigation and water-supply scheme in Stavropol Krai, Russia. The design discharge of 4.0 m^3/s and pool-level difference of 3.5 m are design characteristics. Field values are taken from Zhakapbayeva's Russian-language dissertation (2001) [37], Sections 2.2, 3.1.2–3.1.3, and 3.2.2, using a copy provided by the dissertation's author. No public repository link or formal archival accession number is available for this copy. Original observation logs, calibration data, and related primary records were unavailable; the data-access limitations are summarized in the Data Availability Statement.

Initially, the natural foundation comprised strongly collapsible, silty loess-like sandy soil extending to approximately 19 m below the ground surface, over dense noncollapsible loam. The source reports an initial water content of approximately 0.08, dry density of approximately 1.4 mg/m^3, initial collapse pressure of 25 kPa, and mean collapse strain of 0.067 under natural overburden loading. Wetting was introduced simultaneously from the lined upstream and downstream canal reaches. Opposing wetted zones advanced beneath the structure; their lower parts reportedly met after about 60 days at a depth of approximately 15 m, and the final deformation pattern is reported at day 106. Maintained field water levels, inflow histories, drainage conditions, and moisture-measurement accuracy are not available in the supplied account.

The field structure had no added crossing load. Reported nominal base pressures, dependent on water filling, were 26–30 kPa beneath the inlet, 10–15 kPa beneath the flume, and 29–34 kPa beneath the stilling basin. These are source-reported loading ranges, not a recovered time history of the actual loads or local contact pressures. The 150 kPa model

inlet pressure represented an added crossing-load scenario, so inlet settlements are not compared directly with the field inlet. The two retained field comparison points are the upstream start and downstream end of the stilling basin, with reported settlements of 0.76 and 0.93 m.

Prototype soil collapse-strain versus stress curves informed model mixture selection (Section 2.2). The field comparison therefore does not constitute an independent validation dataset.

The model and source-reported field observations showed qualitatively comparable opposing rotations of the inlet and stilling-basin fragments. At the stilling-basin start, the reported field settlement was 0.76 m and the geometric equivalent of the model settlement was 0.90 m; at the downstream end, the corresponding values were 0.93 and 1.00 m (Figure 4a and Table 7). These two-point comparisons are descriptive. The available records do not permit attribution of the differences to individual causes, establish unit strain similarity, or validate direct settlement scaling.

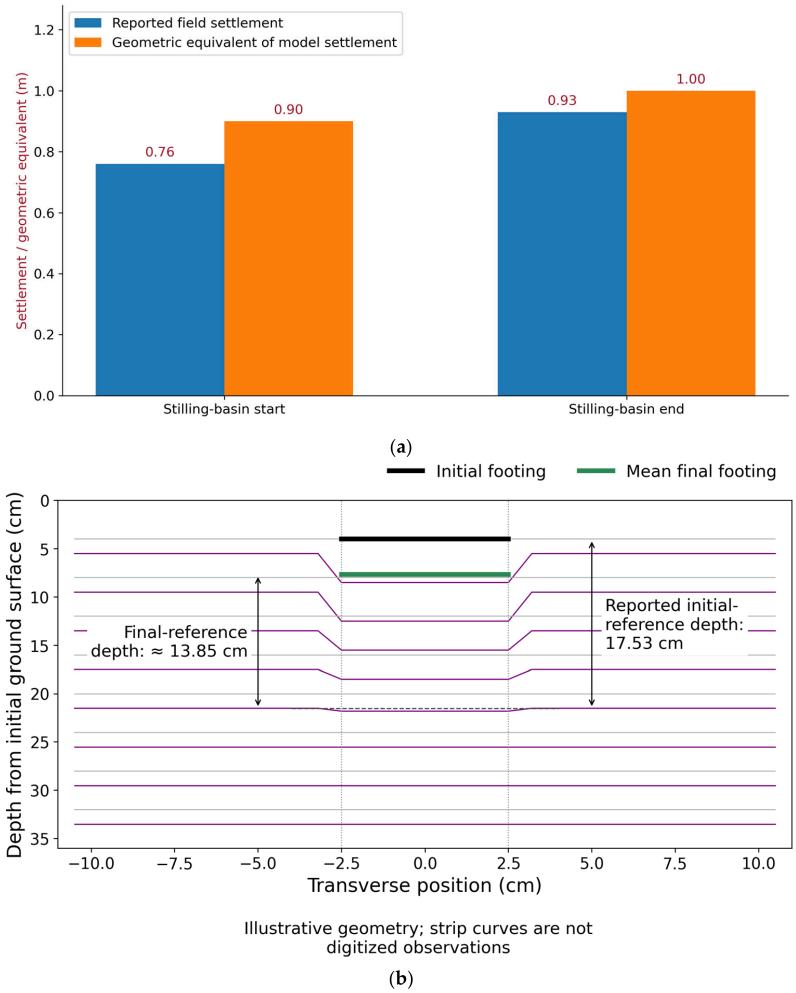


Figure 4. (**a**) Comparison of field settlement with geometric equivalents of measured model settlement. Field settlements and geometric equivalents are in meters; the corresponding measured model settlements are 1.8 and 2.0 cm. Source: Zhakapbayeva (2001) [37]; redrawn or reconstructed for the present article. (**b**) Conceptual indicator-grid scheme showing vertical offsets at the inlet edges and the two depth reference levels. Grey lines indicate initial horizontal strips; purple curves illustrate the reported deformation mechanism, without reproducing measured coordinates. The lower dashed line represents the source-reported boundary; its position and precision have not been independently verified. The 3.68 cm mean settlement changes the reference level only. All plotted lengths are model-scale centimeters. Source: Zhakapbayeva (2001) [37]; redrawn or reconstructed for the present article.

Table 7. Descriptive comparison of field settlements and geometric equivalents of model settlements. Archival model and field data: Zhakapbayeva (2001) [37].

Response	Field or Model-Derived Value	Comparison Value	Absolute Difference; Point-Wise Percentage Difference
Basin-start settlement	0.76 m field	0.90 m geometric equivalent	0.14 m (140 mm); 18.42%
Basin-end settlement	0.93 m field	1.00 m geometric equivalent	0.07 m (70 mm); 7.53%

Note: The field comparisons are descriptive and location-specific.

Both comparison locations are spatial observations within the same stilling-basin segment and field experiment. The source reports the final deformation pattern at day 106. The settlements are source-reported final values; their measurement uncertainty and synchronization with model hydraulic conditions cannot be established.

The comparison is reported separately for each location. At the stilling-basin start, the absolute settlement difference is $|0.90 - 0.76| = 0.14$ m (140 mm), and the point-wise absolute percentage difference is $100 \times 0.14/0.76 = 18.42\%$. At the stilling-basin end, the absolute difference is $|1.00 - 0.93| = 0.07$ m (70 mm), and the point-wise absolute percentage difference is $100 \times 0.07/0.93 = 7.53\%$. In both cases the geometric equivalent exceeds the reported field settlement. The field value at each location is the denominator for its percentage difference. Here, 0.90 and 1.00 m are geometric equivalents, not independently validated prototype predictions. No average error metric is used. With only two locations from the same segment and no measurement-error estimates, these discrepancies provide neither statistical generalization nor validation of a settlement-prediction method. The exact arithmetic differences reflect the reported values and do not establish measurement accuracy.

The source identified the lower extent of localized punching from the progressive reduction with depth of the vertical offsets in horizontal indicator strips at the inlet edges. Figure 4b illustrates this interpretation. Horizontal strips were initially spaced at 4 cm; vertical strips near the footing edges were spaced at 1 cm. The source reports an average depth of 17.53 cm from the initial footing level across three inlet sections. Individual section depths, strip coordinates, an offset-detection threshold, and the interpolation procedure are unavailable. This is a source-reported graphical estimate, not a measurement verified to 0.01 cm.

The reference-level adjustment is hfinal = hinitial − smean. Using the final inlet readings in Table 4 gives smean = (4.50 + 3.87 + 3.55 + 2.81)/4 = 3.6825 cm ≈ 3.68 cm. Consequently, hfinal = 17.53 − 3.6825 = 13.8475 cm ≈ 13.85 cm. Its geometric equivalent is 50 × 13.8475/100 = 6.92375 m ≈ 6.92 m; this is an illustrative length conversion, not a prototype-depth prediction. The source associates 3.71 cm with a central-section average, but does not supply the corresponding paired readings. It is therefore not used as the four-marker mean. Throughout this comparison, measured model lengths are in cm and field lengths or geometric equivalents are in m: Lgeometric (m) = 50 × Lmodel (cm)/100. Thus, the initial-reference model depth of 17.53 cm has a geometric equivalent of 8.765 m (approximately 8.77 m).

The punching-depth estimate is limited by the 4 cm strip spacing, graphical interpolation, and variation between sections. The 0.01 mm surface-reading resolution does not apply to this boundary; the displayed decimals are a result of arithmetic, rather than measurement precision.

3.5. Derived Quantitative Indicators

The derived indicators in Table 8 separate local support loss from load transfer and quantify the spatially nonuniform response. The largest change was the 80.5% unloading at S1, whereas S9 carried 46.7% more than its initial stress. Using midpoint values for the reported ranges, flume-end contact stress decreased by 39.1% and the subsurface vertical pulse increased by 33.9%. Final settlement across the eight reported markers averaged

2.75 cm, with a sample standard deviation of 1.11 cm and a coefficient of variation of 40.2%. This variation describes differences between marker locations within one experiment; it is neither repeat-test scatter nor an estimate of measurement uncertainty.

Table 8. Derived response indicators from the measured and reported values.

Indicator	Basis	Value	Engineering Interpretation
S1 contact unloading	$(154 - 30)/154$	80.5%	Near loss of support in newly wetted soil
S9 dry-side amplification	$(220 - 150)/150$	46.7%	Load transfer to the remaining dry support
Flume-end unloading	$(112.5 - 68.5)/112.5$; midpoints of narrative ranges 110–115 and 67–70 kPa [37]	39.1%	Beam action on the shrinking central support
Subsurface vertical pulse	$(197.5 - 147.5)/147.5$	33.9%	Stress concentration near the wetting front
Lateral stress increase	$(78 - 65)/65$	20.0%	Increased post-collapse confinement
Final-settlement spatial variability	8 markers; mean 2.75 cm; SD 1.11 cm	CV 40.2%	Pronounced differential settlement
Geometric equivalent to field comparison	Basin start/basin end, respectively	0.14 m/0.07 m; 18.42%/7.53%	Point-wise descriptive discrepancies without verified strain similitude

Note: Range midpoints were used only where the original result was reported as a range. The field comparison is reported as separate absolute and percentage differences for each of the two locations; these are descriptive discrepancies, not measurement errors or a validation metric. Specifically, the 39.1% flume-end pressure reduction was calculated using the midpoints of the 110–115 kPa initial range and the 67–70 kPa reduced range reported in the original narrative [37]: $[(112.5 - 68.5)/112.5] \times 100 = 39.1\%$. It was not calculated from the digitized curves in Figure 3b, whose minima are approximately 60–65 kPa.

The experiment was performed once, without independent repeat tests. Marker locations and successive readings from this run are spatially and temporally related observations, not experimental replicates. The spatial coefficient of variation is CV = 100 s/mean settlement, where s is the sample standard deviation across the eight final marker readings. It describes within-test spatial nonuniformity only. A 95% confidence interval for between-test reproducibility cannot be estimated from a single run; treating the eight markers or successive dates as replicates would not provide such an interval. Calibration records also do not permit a separate numerical measurement-uncertainty interval. Accordingly, no inferential significance, population confidence interval, or statistical reproducibility is claimed for the reported indicators. No independent test series at different initial densities or water contents is available; the sensitivity of the reported percentages to these initial conditions therefore cannot be quantified from this dataset.

4. Discussion

4.1. Mechanism of Staged Support Loss

The measurements show why a settlement estimate based only on initial contact pressure can be nonconservative. Collapse is spatially progressive: a wetted zone loses stiffness, the rigid fragment bridges over it, and load transfers to a smaller dry area. The dry loess then carries increased pressure before it is wetted, so collapse develops under a stress greater than the nominal design value. The measured increase from about 150 to 220 kPa is consistent with the strong stress-path dependence reported in controlled wetting tests [7,9–11] and with property evolution inferred from shallow-foundation back-analysis [23].

Differential segment rotation could cause joint opening, and, if watertightness were impaired, could increase leakage and accelerate local wetting. This is a possible feedback mechanism, not a measured outcome of the model experiment. Joint aperture,

rotational capacity, and leakage discharge, as well as their time dependence, were not measured; a causal link between these quantities is therefore not established. Confirming this hypothesis would require synchronized measurements of segment rotation, joint opening, leakage, and local wetting. The literature on coupled wetting and deformation [14–16,20] provides context but does not verify this joint-leakage mechanism in the present test.

The indicator grid supports a qualitative localized punching interpretation, with the depth limitations described in Section 3.4. This does not establish a validated limit-equilibrium solution or imply that every loess foundation can be treated as a Winkler medium. The observations concern a strip-like hydraulic structure, a deeply collapsible profile, and wetting from both ends. Three-dimensional foundations [25], placement history [27], anisotropic fabric, and cyclic wetting [19] require separate assessments.

4.2. Comparison with Previous Research

The results agree with the element-scale literature in showing that wetting-induced deformation cannot be defined by water content alone. Controlled-wetting studies [7–11] identified stress level and wetting path as co-determinants of collapse, while microstructural investigations [12,13,15,19,33] related macroscopic strain to the loss of large pores and inter-aggregate contacts. The present model adds a structural consequence: the stress acting on soil just prior to its wetting is itself modified by deformation of the neighboring wetted zone. In other words, the structure changes the boundary condition of the soil during the collapse process.

Unlike a uniformly loaded oedometer specimen, the segmented structure changes the local stress path as support conditions evolve. The measured redistribution complements the wetting-path studies [7–11] and inverse foundation analysis [23]. It also complements tunnel and storage-foundation studies [21,25] by recording local contact stresses during the transition.

4.3. Qualitative Framework for Staged Assessment

The observations motivate three considerations for further site-specific design assessment. First, calculations could examine transient contact-pressure envelopes, in addition to the initial pressure distribution. Second, watertight joints and drainage details should be treated as geotechnical controls, because they govern the spatial sequence of saturation. Third, the required extent of foundation improvement could be assessed against potential localized collapse zones beneath the footing edges. Instrumented monitoring of joint rotation and differential settlement is particularly valuable during initial filling.

The staged procedure below is a qualitative assessment framework, not a validated calculation method. It organizes questions about probable wetting zones, changes in support, rigid-fragment equilibrium, and the stresses acting on soil prior to its wetting. The experiment does not supply the constitutive relations, contact-area histories, or joint properties needed to predict a complete settlement profile. Quantitative implementation would require site-specific soil characterization, a suitable soil–structure interaction model, and independent verification.

Figure 5 summarizes the stage classification in Section 2.7. Its engineering use is to identify the load-path questions and additional data needed for quantitative analysis. Joint-rotation capacity, watertightness, and field seepage time require separate characterization.

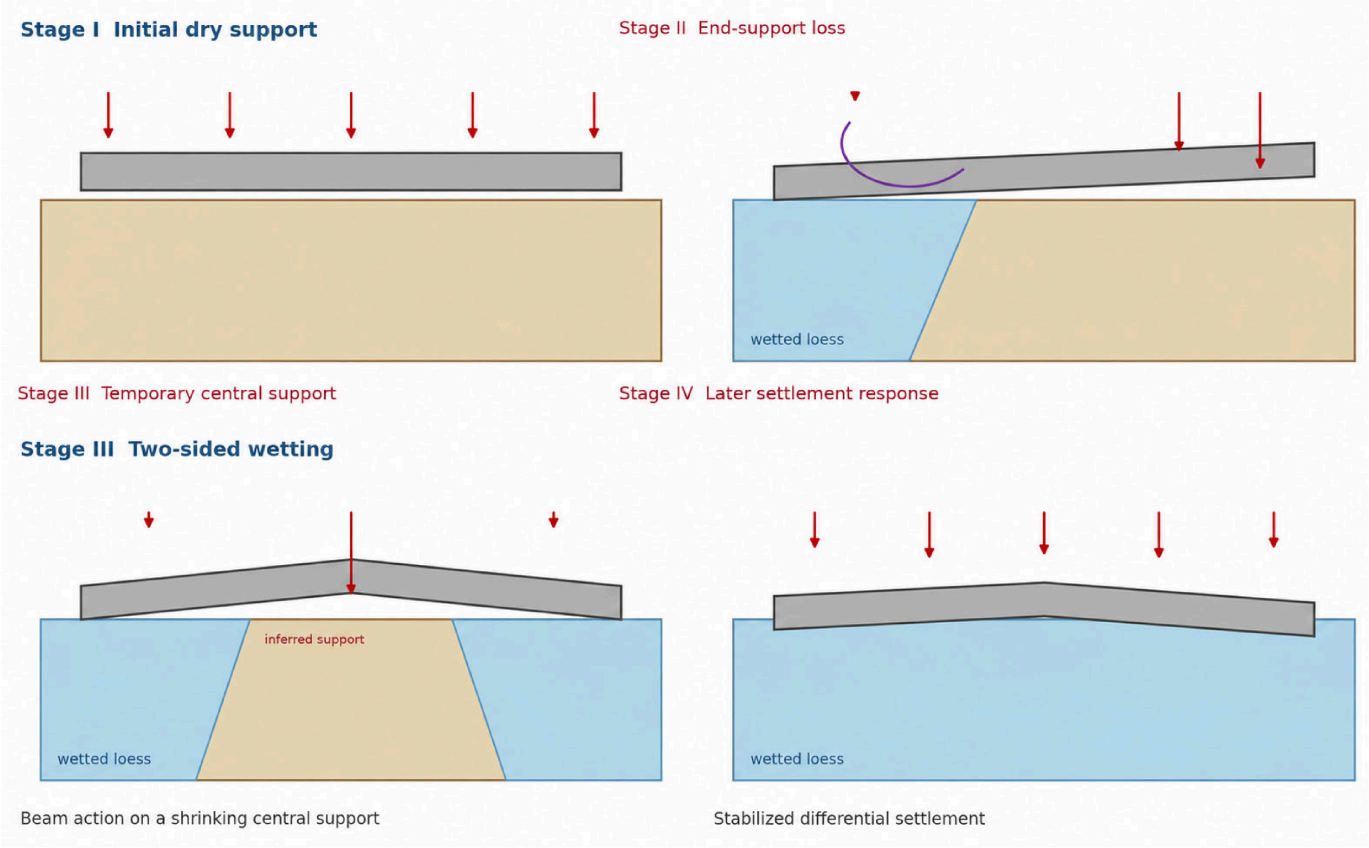


Figure 5. Qualitative interpretation of successive wetting and support configurations; joint opening and increased leakage were not measured. Blue and beige zones illustrate interpreted wetting and support configurations, not measured moisture boundaries; complete foundation saturation was not independently verified. Red downward arrows indicate the applied vertical loading; the purple curved arrow indicates the interpreted rotation of the structure following end-support loss. Arrow lengths are schematic and do not quantify load magnitudes.

4.4. Qualitative Engineering Interpretation of the Measured Stress Path

The model stress changes summarized in Section 3.2 illustrate why a quantitative analysis should account for changing support. The dry-side amplification of approximately 1.47 is specific to this experiment and is not a transferable design factor.

For each configuration in Section 2.7, the analyst should identify the information required to calculate reactions and movements. Joint and waterstop compatibility remain assessment topics requiring separate data.

The established elastic rigidity framework [35] and field evidence on collapsible soil [36] provide context for future quantitative analysis. Neither supplies a validated articulated-chute model; wetting-dependent soil behavior and joint properties must be characterized separately. A beam or plate on deformable support couples structural flexural rigidity to the evolving soil reaction; a continuum soil–structure formulation can represent wetting-dependent constitutive response and changes in contact. For an articulated chute, segment rigidity and joint rotational stiffness must be distinguished: stiff individual fragments do not imply a globally rigid or monolithic structure. Contact loss, changes in support area, force and moment equilibrium, and joint compatibility must be checked together. These are frameworks for interpreting and eventually modelling the observed response, not models calibrated by the present experiment.

The model and source-reported field observations show qualitatively comparable deformation patterns. The field soil characterization also informed model material selec-

tion, so the two settlement points do not constitute independent validation. Geometric equivalents are descriptive only. The principal experimental evidence is the observed redistribution of model contact stresses as support conditions change during wetting.

For other sites, the framework requires site-specific collapse parameters, wetting conditions, foundation geometry, segment stiffness, joint properties, and drainage information. The measured amplification and unloading values should not be transferred directly. The proposed engineering application is qualitative: examine successive support and stress configurations when planning a quantitative analysis.

4.5. Limitations

The experiment represents one loess-based mixture, one structural geometry, and one imposed two-sided wetting scenario without replicate tests. Full geostatic-stress, strain, structural-stiffness, and seepage-time similitude were not established; the miniature box also restricts three-dimensional lateral deformation. The measured stresses and geometric-equivalent deformations therefore cannot be transferred directly to prototype design. Temporary central support remains an interpretation because its pressure and contact area were not measured. Incomplete hydraulic characterization and unavailable primary records, detailed in the Methods and Data Availability Statement, limit independent verification and uncertainty assessment. The model duration cannot be converted into a prototype leakage duration. Localized internal leakage can involve different source locations, discharge histories, and water availability, so its mechanical response requires separate verification.

The spatial coefficient of variation describes settlement differences within this test, and the field comparison comprises only two locations from one experiment. Assessing reproducibility, probabilistic reliability, and transferability requires repeated tests at different initial densities and water contents, representative leakage scenarios, calibrated hydro-mechanical analyses, and field monitoring.

5. Conclusions

1. Two-sided wetting caused a staged change in support conditions beneath the segmented chute rather than uniform settlement under the initial nominal pressure.
2. In this single test, contact stress at the softened S1 support decreased by 80.5%, while stress at the adjacent, initially dry, S9 support increased by 46.7%. These observations suggest that earlier deformation of a neighboring zone can alter the stress path of soil wetted later; the percentages are specific to the tested configuration.
3. Within the same experiment, flume-end stresses decreased by approximately 39%, while the subsurface vertical stress pulse increased by approximately 34%. Beam action on a shrinking temporary central support is proposed as an explanation of the observed flume-end unloading, rather than a directly verified support configuration. As noted in Section 3.2, neither the pressure nor the contact area of this support was measured. These changes are within-test observations and do not establish reproducibility across different initial soil conditions.
4. Final settlement at the eight reported model markers had a spatial coefficient of variation of 40.2%, indicating spatially nonuniform settlement in this test; joint forces and repeat-test variability were not measured.
5. Geometric equivalents of model settlements were compared descriptively with two field observations. The absolute differences were 0.14 m at the stilling-basin start and 0.07 m at its end, with corresponding point-wise percentage differences of 18.42% and 7.53%. The indicator grid supports a localized punching interpretation, but its

boundary-location accuracy is unquantified. These observations do not validate direct prediction of prototype settlements or punching-zone depth under 1 g conditions.

6. The observed stress redistribution motivates a qualitative framework for assessing successive wetting and support configurations. It does not establish a validated design procedure. Independent replicate experiments at different initial densities and water contents are required to assess reproducibility, sensitivity to initial conditions, and transferability before quantitative design application. The proposed link between segment rotation, joint opening, and increased leakage remains a hypothesis requiring separate measurements. Application to internal leakage additionally requires independent characterization of the water source and hydraulic boundary conditions; the observed model time scale is not a prototype leakage time scale.

Author Contributions: Conceptualization, G.Z. (Gulnaz Zhakapbayeva) and S.U.; methodology, G.Z. (Gulnaz Zhakapbayeva) and S.U.; investigation, G.Z. (Gulnaz Zhakapbayeva), G.T. and N.T.; validation, S.U. and N.S.; formal analysis, G.Z. (Gulnaz Zhakapbayeva), A.B. and G.Z. (Gulnur Zhakypova); data curation, G.Z. (Gulnur Zhakypova) and G.T.; visualization, A.B. and G.Z. (Gulnur Zhakypova); writing—original draft preparation, G.Z. (Gulnaz Zhakapbayeva) and S.U.; writing—review and editing, all authors; supervision and project administration, S.U. All authors have read and agreed to the published version of the manuscript.

Funding: This research received no external funding.

Institutional Review Board Statement: Not applicable.

Informed Consent Statement: Not applicable.

Data Availability Statement: The available marker readings, stress summaries, source-reported field values, and approximate graph-derived S10/S12 records used in this analysis are presented in the article and derive from the Russian-language dissertation by Zhakapbayeva (2001) [37], and were based on a copy provided by the dissertation's author. No public repository link or formal archival accession number is available for this copy. Missing early Zh readings are identified in Table 4. Figure 3b contains a graphical reconstruction from [37], not recovered raw numerical readings. Original observation and instrument logs, individual calibration datasets, surveying records, and quantitative moisture/front-coordinate records were unavailable to the authors of the present article. These gaps prevent independent verification of the reconstructed values and their measurement uncertainty. No supplementary dataset or video is provided.

Conflicts of Interest: The authors declare no conflicts of interest.

References

1. Feda, J. Collapse of Loess upon Wetting. *Eng. Geol.* **1988**, *25*, 263–269. [CrossRef]
2. Rogers, C.D.F.; Dijkstra, T.A.; Smalley, I.J. Hydroconsolidation and Subsidence of Loess: Studies from China, Russia, North America and Europe. *Eng. Geol.* **1994**, *37*, 83–113. [CrossRef]
3. Phien-wej, N.; Pientong, G.; Balasubramaniam, A.S. Collapse and Strength Characteristics of Loess in Thailand. *Eng. Geol.* **1992**, *32*, 59–72. [CrossRef]
4. Dudley, J.H. Review of Collapsing Soils. *J. Soil Mech. Found. Div.* **1970**, *96*, 925–947. [CrossRef]
5. Clemence, S.P.; Finbarr, A.O. Design Considerations for Collapsible Soils. *J. Geotech. Eng. Div.* **1981**, *107*, 305–317. [CrossRef]
6. Budikova, A.M.; Kamalova, N.N. Research in Engineering-Geological Characteristics of Forest Soils of the City of Kyzylorda. *Bull. Natl. Acad. Sci. Repub. Kazakhstan* **2021**, *1*, 226–230. [CrossRef]
7. Munoz-Castelblanco, J.; Delage, P.; Pereira, J.M.; Cui, Y.J. Some Aspects of the Compression and Collapse Behaviour of an Unsaturated Natural Loess. *Geotech. Lett.* **2011**, *1*, 17–22. [CrossRef]
8. Munoz-Castelblanco, J.A.; Pereira, J.M.; Delage, P.; Cui, Y.J. The Water Retention Properties of a Natural Unsaturated Loess from Northern France. *Geotechnique* **2012**, *62*, 95–106. [CrossRef]
9. Jiang, M.; Hu, H.; Liu, F. Summary of Collapsible Behaviour of Artificially Structured Loess in Oedometer and Triaxial Wetting Tests. *Can. Geotech. J.* **2012**, *49*, 1147–1157. [CrossRef]

10. Singhal, S.; Sharma, R.S.; Phanikumar, B.R. A Laboratory Study of Collapse Behaviour of Remoulded Loess under Controlled Wetting and Flooding. *Geomech. Geoengin.* **2016**, *11*, 159–163. [CrossRef]
11. Shao, X.; Zhang, H.; Tan, Y. Collapse Behavior and Microstructural Alteration of Remolded Loess under Graded Wetting Tests. *Eng. Geol.* **2018**, *233*, 11–22. [CrossRef]
12. Ge, M.; Pineda, J.A.; Sheng, D.; Burton, G.J.; Li, N. Microstructural Effects on the Wetting-Induced Collapse in Compacted Loess. *Comput. Geotech.* **2021**, *138*, 104359. [CrossRef]
13. Wang, Y.; Li, Y. Wetting-Induced Collapse of Loess: Tracing Microstructural Evolution. *Eng. Geol.* **2024**, *340*, 107673. [CrossRef]
14. Lan, T.G.; Xu, L.; Lu, S.F. Experimental Study on the Water Retention Behavior of Intact Loess under Mechanical Wetting and Hydraulic Wetting. *Acta Geotech.* **2023**, *18*, 1125–1134. [CrossRef]
15. Jian, T.; Kong, L.; Bai, W.; Sun, Z. Investigation on Compressibility and Microstructure Evolution of Intact Loess at Different Wetting States. *Front. Earth Sci.* **2022**, *10*, 923358. [CrossRef]
16. Wang, J.; Zhang, D.; Zhang, Y.; Chen, H.; Ma, W. Variations in Hydraulic Properties of Collapsible Loess Exposed to Wetting and Shearing. *Acta Geotech.* **2022**, *17*, 2995–3015. [CrossRef]
17. Ng, C.W.W.; Cheng, Q.; Zhou, C. Thermal Effects on Yielding and Wetting-Induced Collapse of Recompacted and Intact Loess. *Can. Geotech. J.* **2018**, *55*, 1095–1103. [CrossRef]
18. Mu, Q.; Meng, L.; Lu, Z.; Zhang, L. Hydro-Mechanical Behavior of Unsaturated Intact Paleosol and Intact Loess. *Eng. Geol.* **2023**, *323*, 107245. [CrossRef]
19. Ni, W.; Yuan, K.; Lu, X.; Yuan, Z. Comparison and Quantitative Analysis of Microstructure Parameters between Original and Remoulded Loess under Different Wetting-Drying Cycles. *Sci. Rep.* **2020**, *10*, 5547. [CrossRef]
20. Hong, Q.; Lai, H.; Liu, Y. Mechanical and Permeability Characteristics of Q2 Soft-Plastic Loess under Coupled Hydro-Mechanical Conditions. *Environ. Earth Sci.* **2024**, *83*, 75. [CrossRef]
21. Weng, X.; Sun, Y.; Zhang, Y.; Niu, H.; Liu, X.; Dong, Y. Physical Modeling of Wetting-Induced Collapse of Shield Tunneling in Loess Strata. *Tunn. Undergr. Space Technol.* **2019**, *90*, 208–219. [CrossRef]
22. Jiang, M.; Li, T.; Thornton, C.; Hu, H. Wetting-Induced Collapse Behavior of Unsaturated and Structural Loess under Biaxial Tests Using Distinct Element Method. *Int. J. Geomech.* **2017**, *17*, 04016030. [CrossRef]
23. Francisca, F.M.; Giomi, I.; Rocca, R.J. Inverse Analysis of Shallow Foundation Settlements on Collapsible Loess: Understanding the Impact of Varied Soil Mechanical Properties during Wetting. *Comput. Geotech.* **2024**, *167*, 106090. [CrossRef]
24. Piyasawat, K.; Nuntasarn, R.; Hormdee, D.; Punrattanasin, P. Bearing Capacity of Shallow Foundation on Collapsible Khon Kaen Loess. *Int. J. GEOMATE* **2021**, *20*, 159–167. [CrossRef]
25. Huang, W.; Cao, X.; Xie, H.; Sun, H.; Cheng, X. Seismic Response of Foundation Settlement for Liquid Storage Structure in Collapsible Loess Areas. *Appl. Sci.* **2024**, *14*, 8993. [CrossRef]
26. Zhang, L.; Li, T.; Zhang, Y. A Simple Method for Predicting Wetting-Induced Collapse Behavior of Compacted Loess with Various Initial Void Ratios and Moisture Contents. *Environ. Earth Sci.* **2023**, *82*, 24. [CrossRef]
27. Lan, H.; Zhang, T.; Peng, J.; Zhang, F.; Li, L.; Wu, Y.; Tian, N.; Clague, J.J. Large Scale Land Reclamation and the Effects on Hydro-Mechanical Behavior in Loess and Loess-Derived Fill. *Eng. Geol.* **2023**, *323*, 107241. [CrossRef]
28. Tang, C.; Pan, X.; Cheng, Y.; Ji, X. Improving Hydro-Mechanical Behavior of Loess by a Bio-Strategy. *Biogeotechnics* **2023**, *1*, 100024. [CrossRef]
29. Cui, S.; Xie, W.; Wang, J.; Huang, S. Engineering Properties of Collapsible Loess Stabilized by Cement Kiln Dust. *Soil Mech. Found. Eng.* **2019**, *56*, 328–335. [CrossRef]
30. Cai, J.; Zhang, J.; Du, G.; Xia, H. Application of the Dynamic Compaction Method for Ground Improvement of Collapsible Loess in Qinhai. *Tek. Dergi* **2022**, *33*, 11455–11472. [CrossRef]
31. Shao, Y.; Yuan, M.; Hao, Y.; Sun, X. Laboratory Test Research on Collapsible Loess Foundation Treatment. *E3S Web Conf.* **2020**, *194*, 05065. [CrossRef]
32. Hou, J.; Lu, Y.; Wang, J.; Yu, K. Calculation Model of Compaction Coefficient of Soil among SP-PSC Pile Group on Collapsible Loess Foundation. *Appl. Sci.* **2023**, *13*, 4003. [CrossRef]
33. Wang, M.; Bai, X. Collapse Property and Microstructure of Loess. In *Advances in Unsaturated Soil, Seepage, and Environmental Geotechnics*; ASCE: Reston, VA, USA, 2006; pp. 111–118. [CrossRef]
34. *ASTM D4546-25*; Standard Test Methods for One-Dimensional Swell or Collapse of Soils. ASTM International: West Conshohocken, 2025.
35. Mayne, P.W.; Poulos, H.G. Approximate Displacement Influence Factors for Elastic Shallow Foundations. *J. Geotech. Geoenvironmental Eng.* **1999**, *125*, 453–460. [CrossRef]

36. Martins, P.V.N.; Dias Filho, J.L.E.; Carvalho, L.G.; Sousa, M.A.P.; Kühn, V.O. Settlement Monitoring of Shallow Foundations in Collapsible Tropical Soil. *Soils Rocks* **2026**, *49*, e2026009724. [CrossRef]
37. Zhakapbayeva, G.A. Improvement of Design Methods for Irrigation-System Structures on Collapsible Soils Based on Joint Limit Deformations. Ph.D. Thesis, Moscow State University of Environmental Engineering, Moscow, Russia, 2001. (In Russian)

Disclaimer/Publisher's Note: The statements, opinions and data contained in all publications are solely those of the individual author(s) and contributor(s) and not of MDPI and/or the editor(s). MDPI and/or the editor(s) disclaim responsibility for any injury to people or property resulting from any ideas, methods, instructions or products referred to in the content.